

Microwave Radar and Microwave-Induced Thermoacoustics: Dual-Modality Approach for Breast Cancer Detection

Evgeny Kirshin*, Borislav Oreshkin, Guangran Kevin Zhu, Milica Popović, and Mark Coates

Abstract—Microwave radar and microwave-induced thermoacoustics, recently proposed as promising breast cancer detection techniques, each have shortcomings that reduce detection performance. Making the assumption that the measurement noises experienced when applying these two techniques are independent, we propose a methodology to process the input signals jointly based on a hypothesis testing framework. We present two test statistics and derive their distributions to set the thresholds. The methodology is evaluated on numerically simulated signals acquired from 2-D numerical breast models using finite-difference time-domain method. Our results show that the proposed dual-modality approach can give a significant improvement in detection performance.

Index Terms—Breast, breast cancer detection, hypothesis testing, imaging, microwave, sensor fusion, ultrawide band (UWB).

I. INTRODUCTION

SEVERAL promising microwave breast cancer detection techniques have been under development for the past decade. Among them are ultrawide band microwave radar (MR) imaging and microwave-induced thermoacoustics (MIT) [1], [2]. These techniques are intended to complement conventional methods such as X-ray mammography and magnetic resonance imaging (MRI).

MR breast imaging exploits the contrast in the dielectric properties between malignant and healthy tissues by radiating subnanosecond microwave pulses to the breast and collecting the scattered energy. As the malignant tissue commonly has higher permittivity than ambient healthy tissue, more microwave energy is reflected at its location. This method forms images of scattered microwave energy. MIT breast imaging exploits the contrast in the conductive loss between malignant and healthy

tissue and holds the promise of a high spatial resolution due to the short acoustic wavelength [2], [3]. The MIT technique involves illuminating the breast with microwaves to achieve selective heating of tumorous areas due to the contrast in the conductive loss. This leads to expansion of these areas, which produces acoustic waves, recorded with transducers. Processing of the collected signals gives the images, representing the absorption of microwave energy inside the breast.

A number of significant steps have been made to address the essential problems related to the MR and MIT detection modalities. Fear *et al.* proposed one of the first MR breast cancer detection systems in [1]; the delay-and-sum algorithm was used for imaging and detection. Bond *et al.* developed beamforming algorithms [4] and Davis *et al.* developed hypothesis testing algorithms [5]. Williams *et al.* developed complementary processing techniques including artifact removal and skin surface identification [6]. Klemm *et al.* [7] described an experimental system and reported on its evaluation on realistic breast models and patients. Xie *et al.* strived to improve the robustness of detection for the MR method in [8]; a similar methodology was applied to the MIT modality in [9]. Xu and Wang demonstrated the feasibility of the MIT technique for imaging biological tissues in [3], and Kruger *et al.* described the first hardware device for MIT-based breast imaging in [2].

Recent experimental works, however, show that certain challenges remain unresolved or resolved only partially, which demands further investigations in the field of microwave breast cancer detection. The major problems associated with MR and MIT techniques are the high level of tissue heterogeneity for MR and uneven heating for the MIT. These lead to clutter in the generated images and the potential for false positives. To the best of our knowledge, no attempts have been made to fuse the MR and MIT modalities together into a single imaging system, which is the purpose of this paper. We employ the assumption that the measurement noises experienced when applying these two techniques are independent because they rely on different physical characteristics. We propose a methodology to process the input signals jointly based on a hypothesis testing framework and propose two different test statistics. In order to set the threshold for detection, we derive the null distributions of the test statistics. We evaluate our methodology on numerically simulated signals acquired by applying the finite-difference time-domain (FDTD) method to a set of 2-D breast models. These models have a realistic distribution of tissue derived from MRI images. The results of our dual-modality system demonstrate significant improvement in the detection performance.

Manuscript received November 21, 2011; revised June 23, 2012; accepted September 11, 2012. Date of publication November 12, 2012; date of current version January 16, 2013. This work was supported by the National Science and Engineering Research Council of Canada and Partnerships for Research on Microelectronics, Photonics and Telecommunications, QC, Canada. *Asterisk indicates corresponding author.*

*E. Kirshin is with the Department of Electrical and Computer Engineering, McGill University, Montreal, QC H2X 2B6, Canada (e-mail: evgeny.kirshin@gmail.com).

B. Oreshkin, G. K. Zhu, M. Popović, and M. Coates are with the Department of Electrical and Computer Engineering, McGill University, Montreal, QC H3A 0E9, Canada (e-mail: boris.oreshkin@mail.mcgill.ca; kzhu@waves.utoronto.ca; milica.popovich@mcgill.ca; mark.coates@mcgill.ca).

Color versions of one or more of the figures in this paper are available online at <http://ieeexplore.ieee.org>.

Digital Object Identifier 10.1109/TBME.2012.2220768

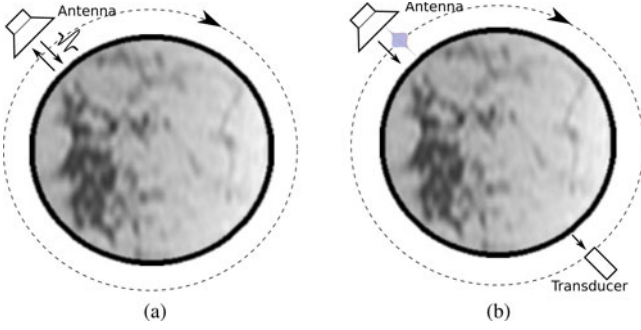


Fig. 1. Schematic representation of the proposed dual-modality breast cancer detection method. (a) MR mode. (b) MIT mode.

The rest of this paper is organized as follows. Section II presents the dual-modality detection scheme and defines the problems we address. The details of our methodology are provided in Section III. The numerical simulation evaluation process is described in Section IV. Implementation details and the results are discussed in Section V. Finally, we conclude this paper with Section VI.

We denote vectors and matrices with boldface lower and upper case symbols, respectively. Superscripts T , H , and -1 denote the transpose, the conjugate transpose, and the inverse, respectively.

II. PROBLEM STATEMENT

In our breast cancer detection problem we consider a scenario in which a patient lies on a test bed in a prone position with the breast naturally hanging down into an aperture with antennas and acoustic transducers surrounding the breast. Fig. 1 shows a simplified dual-modality detection scheme as a coronal slice of one of the breasts of the patient and one of the antennas/acoustic transducers.

We consider a two-stage data acquisition system. At the first stage, the system works in the MR mode [see Fig. 1(a)]: sequentially for each of M_1 antennas, a wideband microwave pulse is radiated toward the breast and the reflected signal is collected with the same antenna (recorded in N_1 samples).

At the second stage (MIT mode), 800-MHz microwave-modulated pulses of a microsecond duration are radiated to heat the breast from M_2 angles. The induced acoustic signals are received by the transducer on the opposite side of the breast (N_2 samples). The MIT mode requires a relatively large acoustic transducer to receive the signals; the alternative, simpler scenario can be implemented with just one microwave antenna and one acoustic transducer at the opposite side of the breast [as suggested in Fig. 1(b)], rotated mechanically around the breast.

Signals recorded for both MR and MIT modes have several contributions. In the MR case, signals contain incident antenna pulses, reflections from the skin-breast interface, reflections from the internal tissue (clutter) as well as the measurement noise. Similar contributions are relevant for the MIT signals, except for the incident pulse, since the MIT signals are induced rather than reflected. The incident antenna pulses are removed from the MR signals by subtracting the known calibration signal

(recorded beforehand without the patient on the test bed). In our study, we extend the algorithm by Bond *et al.* [4] and employ it to remove the skin-breast artifacts from both the MR and MIT signals.

After the preprocessing procedures, we have a set of column-vectors $\mathbf{x}_i = [x_{i,1}, \dots, x_{i,N_1}]^T$, $i = 1 \dots M_1$ which represent the MR signals and another set of column-vectors $\mathbf{y}_j = [y_{j,1}, \dots, y_{j,N_2}]^T$, $j = 1 \dots M_2$ for the MIT signals. A case with $N_1 = N_2 = N$ and $M_1 = M_2 = M$ is considered further in this paper.

In our study, we adopt the detection-theoretic approach of hypothesis testing, based on the analysis of a test statistic, and search for the optimal way to process jointly the signals \mathbf{x}_i and \mathbf{y}_j . We derive a test statistic for the dual-modality approach and its null-hypothesis distribution for the purpose of setting a threshold for detection. For assessment purposes, MR and MIT single-modality test statistics are also computed. We evaluate the dual-modality approach on a set of signals acquired from numerical simulations of the described test bed. Structurally realistic breast models with multiple settings of the dielectric tissue properties are constructed for the simulations to examine the impact of low contrast and high clutter.

III. METHODOLOGY

A. Signal Models and Assumptions

We consider scanning the breast interior by modeling the location of the tumor as taking one of a finite set of locations $\{\mathbf{r}_\ell\}$, $\ell = 1, \dots, L$. Index ℓ_t denotes the “true” location, if the tumor exists. Signals \mathbf{x}_i and \mathbf{y}_j can then be modeled as a combination of scaled signals $\mathbf{s}_i(\boldsymbol{\theta}_{\ell_t})$ (scattered microwave signal from a tumor) and $\mathbf{d}_j(\boldsymbol{\theta}_{\ell_t})$ (pressure signal induced by a tumor) with the corresponding noise components $\boldsymbol{\xi}_i$ and $\boldsymbol{\zeta}_j$

$$\mathbf{x}_i = \beta_{\ell_t} \mathbf{s}_i(\boldsymbol{\theta}_{\ell_t}) + \boldsymbol{\xi}_i, \quad i = 1, \dots, M \quad (1)$$

$$\mathbf{y}_j = \eta_{\ell_t} \mathbf{d}_j(\boldsymbol{\theta}_{\ell_t}) + \boldsymbol{\zeta}_j, \quad j = 1, \dots, M. \quad (2)$$

The vector of parameters $\boldsymbol{\theta}_\ell$ incorporates the tissue and geometry properties that affect the propagation and shape of the received signals. These properties are estimated at the preprocessing stage and considered to be known in this context. Signal amplitudes β_ℓ and η_ℓ are treated as unknown deterministic parameters; the signals $\mathbf{s}_i(\boldsymbol{\theta}_\ell)$, $\mathbf{d}_j(\boldsymbol{\theta}_\ell)$ are treated as deterministic and dependent on a set of parameters $\boldsymbol{\theta}_\ell$. Thus, for any given location \mathbf{r}_ℓ , we consider \mathbf{s} and \mathbf{d} as known and refer to them as “signal templates” (the construction of signal templates is described in detail in Section III-E).

We model the noise components $\boldsymbol{\xi}_i$ and $\boldsymbol{\zeta}_j$ as jointly Gaussian with zero means and covariances $\sigma_\xi^2 \mathbf{R}_\xi$ and $\sigma_\zeta^2 \mathbf{R}_\zeta$, where matrices \mathbf{R}_ξ and \mathbf{R}_ζ capture the structural properties of the covariance, and scalars σ_ξ^2 and σ_ζ^2 specify the noise powers. The noise components are assumed to be independent between the channels and between the MR and MIT methods. We assume that \mathbf{R}_ξ and \mathbf{R}_ζ can be estimated using a training dataset containing responses from a number of healthy breasts.

We further refer to a concatenation of vectors \mathbf{x}_i as to a single NM-length vector \mathbf{x} . Similarly, vectors \mathbf{y} , \mathbf{s} , and \mathbf{d} represent

NM-length vectors of concatenated vectors \mathbf{y}_j , \mathbf{s}_i , and \mathbf{d}_j respectively.

B. Hypothesis Testing and Generalized Likelihood Ratio Test (GLRT)

At each scan location $\{\mathbf{r}_\ell\}_{\ell=1}^L$, we consider a binary hypothesis test of a tumor presence (hypothesis $\mathcal{H}_\ell^{(1)}$) versus null-hypothesis ($\mathcal{H}_\ell^{(0)}$) for the joint MR/MIT breast tumor detection as follows:

$$\mathcal{H}_\ell^{(0)} : \beta_\ell, \eta_\ell = 0 \text{ versus } \mathcal{H}_\ell^{(1)} : \beta_\ell, \eta_\ell \neq 0. \quad (3)$$

According to our signal models (1), (2) and assumptions described earlier, we are faced with the detection problem of a known signal (up to a scaling factor) with the noise of unknown parameters. To address this problem, a theoretical framework has been previously developed and is known as the GLRT [10].

The GLRT for classical linear model with unknown σ^2 is derived with the assumption of white noise [10, Th. 9.1]. Thus, prior to the application of the algorithm, the input signals \mathbf{x} and \mathbf{y} are whitened using the estimated clutter covariance matrices

$$\tilde{\mathbf{x}} = \hat{\mathbf{R}}_\xi^{-1/2} \mathbf{x}; \quad \tilde{\mathbf{y}} = \hat{\mathbf{R}}_\zeta^{-1/2} \mathbf{y}. \quad (4)$$

The clutter covariance matrices are estimated from a training set of available ten tumor-free breasts, using the averaging approach described in [5]. In order to compensate for the distortion introduced by whitening, we expose the signal templates to the same whitening procedure, which produces $\tilde{\mathbf{s}}$ and $\tilde{\mathbf{d}}$ vectors.

The GLRT performs the comparison of the generalized likelihood ratio $L_G(\tilde{\mathbf{x}}, \tilde{\mathbf{y}})$ against a threshold γ

$$L_G(\tilde{\mathbf{x}}, \tilde{\mathbf{y}}) \underset{\mathcal{H}_\ell^{(0)}}{\overset{\mathcal{H}_\ell^{(1)}}{\geq}} \gamma. \quad (5)$$

$L_G(\tilde{\mathbf{x}}, \tilde{\mathbf{y}})$ can be factorized under the assumption that the noises are independent

$$L_G(\tilde{\mathbf{x}}, \tilde{\mathbf{y}}) = \frac{p(\tilde{\mathbf{x}}|\hat{\beta}_{\ell_1}, \hat{\sigma}_{\xi, \ell_1}^2, \mathcal{H}_1) \cdot p(\tilde{\mathbf{y}}|\hat{\eta}_{\ell_1}, \hat{\sigma}_{\zeta, \ell_1}^2, \mathcal{H}_1)}{p(\tilde{\mathbf{x}}|\hat{\sigma}_{\xi, \ell_0}^2, \mathcal{H}_0) \cdot p(\tilde{\mathbf{y}}|\hat{\sigma}_{\zeta, \ell_0}^2, \mathcal{H}_0)} \quad (6)$$

where subindices ℓ_1 and ℓ_0 denote the corresponding quantities for the scenario with and without a tumor at the location number ℓ , respectively. Maximum likelihood estimates (MLE) for the unknown variables are given by [10, Appendix 9A]

$$\hat{\beta}_{\ell_1} = (\tilde{\mathbf{s}}^H \tilde{\mathbf{s}})^{-1} \tilde{\mathbf{s}}^H \tilde{\mathbf{x}}; \quad \hat{\eta}_{\ell_1} = (\tilde{\mathbf{d}}^H \tilde{\mathbf{d}})^{-1} \tilde{\mathbf{d}}^H \tilde{\mathbf{y}}; \quad (7)$$

$$\hat{\sigma}_{\xi, \ell_1}^2 = \frac{1}{\text{NM}} \tilde{\mathbf{x}}^H (\mathbf{I} - \mathbf{P}_{\tilde{\mathbf{s}}}) \tilde{\mathbf{x}}; \quad \hat{\sigma}_{\xi, \ell_0}^2 = \frac{1}{\text{NM}} \tilde{\mathbf{x}}^H \tilde{\mathbf{x}}; \quad (8)$$

$$\hat{\sigma}_{\zeta, \ell_1}^2 = \frac{1}{\text{NM}} \tilde{\mathbf{y}}^H (\mathbf{I} - \mathbf{P}_{\tilde{\mathbf{d}}}) \tilde{\mathbf{y}}; \quad \hat{\sigma}_{\zeta, \ell_0}^2 = \frac{1}{\text{NM}} \tilde{\mathbf{y}}^H \tilde{\mathbf{y}}. \quad (9)$$

In these expressions, \mathbf{I} denotes the identity matrix and $\mathbf{P}_{\tilde{\mathbf{s}}} = \tilde{\mathbf{s}}(\tilde{\mathbf{s}}^H \tilde{\mathbf{s}})^{-1} \tilde{\mathbf{s}}^H$ and $\mathbf{P}_{\tilde{\mathbf{d}}} = \tilde{\mathbf{d}}(\tilde{\mathbf{d}}^H \tilde{\mathbf{d}})^{-1} \tilde{\mathbf{d}}^H$ represent projection matrices that project a vector onto the signal subspace.

Making use of the MLE expressions in (6) and considering Gaussian distributions, results in

$$\begin{aligned} L_G(\tilde{\mathbf{x}}, \tilde{\mathbf{y}}) &= \left(\frac{\hat{\sigma}_{\xi, \ell_0}^2}{\hat{\sigma}_{\xi, \ell_1}^2} \right)^{\frac{\text{NM}}{2}} \cdot \left(\frac{\hat{\sigma}_{\zeta, \ell_0}^2}{\hat{\sigma}_{\zeta, \ell_1}^2} \right)^{\frac{\text{NM}}{2}} \\ &= \left(\frac{\tilde{\mathbf{x}}^H \tilde{\mathbf{x}}}{\tilde{\mathbf{x}}^H (\mathbf{I} - \mathbf{P}_{\tilde{\mathbf{s}}}) \tilde{\mathbf{x}}} \right)^{\frac{\text{NM}}{2}} \cdot \left(\frac{\tilde{\mathbf{y}}^H \tilde{\mathbf{y}}}{\tilde{\mathbf{y}}^H (\mathbf{I} - \mathbf{P}_{\tilde{\mathbf{d}}}) \tilde{\mathbf{y}}} \right)^{\frac{\text{NM}}{2}} \\ &= (\Lambda(\tilde{\mathbf{x}}) \cdot \Lambda(\tilde{\mathbf{y}}))^{\frac{\text{NM}}{2}}. \end{aligned} \quad (10)$$

Substituting this into (5) and noting that $(\cdot)^{\frac{\text{NM}}{2}}$ is a monotonically increasing function results in the following decision rule:

$$Z'(\tilde{\mathbf{x}}, \tilde{\mathbf{y}}) = \Lambda(\tilde{\mathbf{x}}) \cdot \Lambda(\tilde{\mathbf{y}}) \underset{\mathcal{H}_\ell^{(0)}}{\overset{\mathcal{H}_\ell^{(1)}}{\geq}} \gamma'. \quad (11)$$

For a fixed probability of false alarm, the threshold γ' can be determined from the inverse cumulative distribution function (CDF) of the test statistic $Z'(\tilde{\mathbf{x}}, \tilde{\mathbf{y}})$ (see Section III-D).

It can be shown that $Z'(\tilde{\mathbf{x}}, \tilde{\mathbf{y}})$ can be expanded as follows:

$$Z'(\tilde{\mathbf{x}}, \tilde{\mathbf{y}}) = 1 + U(\tilde{\mathbf{x}})V(\tilde{\mathbf{y}}) + U(\tilde{\mathbf{x}}) + V(\tilde{\mathbf{y}}) \quad (12)$$

where

$$U(\tilde{\mathbf{x}}) = \frac{\tilde{\mathbf{x}}^H \mathbf{P}_{\tilde{\mathbf{s}}} \tilde{\mathbf{x}}}{\tilde{\mathbf{x}}^H \mathbf{P}_{\tilde{\mathbf{s}}}^\perp \tilde{\mathbf{x}}}; \quad V(\tilde{\mathbf{y}}) = \frac{\tilde{\mathbf{y}}^H \mathbf{P}_{\tilde{\mathbf{d}}} \tilde{\mathbf{y}}}{\tilde{\mathbf{y}}^H \mathbf{P}_{\tilde{\mathbf{d}}}^\perp \tilde{\mathbf{y}}} \quad (13)$$

are separate test statistics for MR and MIT modalities, respectively, and $\mathbf{P}^\perp = \mathbf{I} - \mathbf{P}$. Test statistic $U(\tilde{\mathbf{x}})$ is derived in [5]. In order to eliminate the bias term in Z' , the constant 1 is subtracted from it, which results in

$$Z(\tilde{\mathbf{x}}, \tilde{\mathbf{y}}) = U(\tilde{\mathbf{x}})V(\tilde{\mathbf{y}}) + U(\tilde{\mathbf{x}}) + V(\tilde{\mathbf{y}}). \quad (14)$$

C. Heuristic Test Statistic

In our study, we also consider a heuristic alternative to $Z(\tilde{\mathbf{x}}, \tilde{\mathbf{y}})$. Since U and V are likelihood ratios, it is intuitive to multiply them to fuse the results of the MR and MIT modes

$$W(\tilde{\mathbf{x}}, \tilde{\mathbf{y}}) = U(\tilde{\mathbf{x}}) \cdot V(\tilde{\mathbf{y}}). \quad (15)$$

Later in Section V we show that in our experiments the $W(\tilde{\mathbf{x}}, \tilde{\mathbf{y}})$ statistic provides higher clutter and sidelobe suppression performance than the derived $Z(\tilde{\mathbf{x}}, \tilde{\mathbf{y}})$.

D. Distributions of the Test Statistics

The distribution of $U(\tilde{\mathbf{x}})$ and $V(\tilde{\mathbf{y}})$ up to a scaling constant under \mathcal{H}_0 is given in [10] and is identified to be the central-F with the same degrees of freedom, $c_1 = c_2 = 1$ for the numerator and $d_1 = d_2 = (\text{NM} - 1)$ for the denominator. Detailed derivation for the CDFs of $W(\tilde{\mathbf{x}}, \tilde{\mathbf{y}})$ and $Z(\tilde{\mathbf{x}}, \tilde{\mathbf{y}})$ is available in [11].

In brief, the expression for the CDF of $Z(\tilde{\mathbf{x}}, \tilde{\mathbf{y}})$ is obtained by considering $Z(\tilde{\mathbf{x}}, \tilde{\mathbf{y}})$ in the form of (11) and representing it as a product of two identically distributed random variables Z_i of the form $Z_i = (Y_i + X_i)/Y_i$ with $Y_i = \tilde{\mathbf{x}}_i^H \mathbf{P}_{\tilde{\mathbf{s}}}^\perp \tilde{\mathbf{x}}_i$ and $X_i = \tilde{\mathbf{x}}_i^H \mathbf{P}_{\tilde{\mathbf{s}}} \tilde{\mathbf{x}}_i$. Under \mathcal{H}_0 , they are independent, central chi-square distributed random variables with c_i and d_i degrees of freedom, respectively.

By considering the joint distribution of numerator $\omega = X + Y$ and denominator $\alpha = Y$ and using the Jacobian method for the random variable transformation, the probability density function of Z_i can be represented in terms of Meijer's G-function as follows:

$$p_{Z_i}(z_i) = \frac{\Gamma(\frac{c_i}{2} + \frac{d_i}{2})}{\Gamma(\frac{c_i}{2})} G_{1,1}^{0,1} \left(z_i \left| \begin{array}{c} -\frac{c_i}{2} \\ -\frac{c_i}{2} - \frac{d_i}{2} \end{array} \right. \right) \quad (16)$$

where Γ denotes the Gamma-function and G is Meijer's G-function [12].

Applying the Jacobian technique again and using the G-function integrating formulas from [12], it can be shown that the CDF of $Z = Z_1 Z_2$ is

$$P_Z(z) = \frac{\Gamma(\frac{c_1}{2} + \frac{d_1}{2})\Gamma(\frac{c_2}{2} + \frac{d_2}{2})}{\Gamma(\frac{c_1}{2})\Gamma(\frac{c_2}{2})} \cdot G_{3,3}^{0,3} \left(z \left| \begin{array}{ccc} 1 - \frac{c_1}{2}, & 1 - \frac{c_2}{2}, & 1 \\ 1 - \frac{c_1}{2} - \frac{d_1}{2}, & 1 - \frac{c_2}{2} - \frac{d_2}{2}, & 0 \end{array} \right. \right). \quad (17)$$

The distribution of $W(\tilde{\mathbf{x}}, \tilde{\mathbf{y}})$ under \mathcal{H}_0 is the distribution of the product of two centered F-distributed random variables, which can also be expressed in terms of chi-square distributions. The procedure of the derivations uses similar techniques to ones employed for the $P_Z(z)$ derivation. We obtain the moment generating function for W and express it in terms of Meijer's G-functions as follows:

$$M_W(\omega) = \frac{G_{3,2}^{2,3} \left(\frac{d_1 d_2}{c_1 c_2 \omega} \left| \begin{array}{c} 1, 1 - \frac{c_1}{2}, 1 - \frac{c_2}{2} \\ \frac{d_1}{2}, \frac{d_2}{2} \end{array} \right. \right)}{\Gamma(d_1/2)\Gamma(d_2/2)\Gamma(c_1/2)\Gamma(c_2/2)} \quad (18)$$

where c_1, c_2, d_1 , and d_2 are the degrees of freedom of the four chi-square random variables.

The inverse Laplace transformation of (18) and application of the formulas from [12] give the expression of the CDF

$$P_W(w) = \frac{G_{3,3}^{2,3} \left(\frac{d_1 d_2}{c_1 c_2} w \left| \begin{array}{ccc} 1 - \frac{c_1}{2}, & 1 - \frac{c_2}{2}, & 1 \\ \frac{d_1}{2}, & \frac{d_2}{2}, & 0 \end{array} \right. \right)}{\Gamma(d_1/2)\Gamma(d_2/2)\Gamma(c_1/2)\Gamma(c_2/2)}. \quad (19)$$

E. Signal Templates

The parameter $\boldsymbol{\theta}_\ell$ denotes a vector whose elements are the estimated tissue and geometric properties that affect the MR and MIT signal templates. For the MR signal template, the elements include the estimated Debye parameters of average breast tissue. The signal template models both the propagation and scattering of the microwave pulse. Its frequency-domain representation is

$$\mathbf{S}_i(\boldsymbol{\theta}_\ell, \omega) = G(j\omega) \frac{e^{-2jk_{bg}(\omega)d_{bg,i}}}{\sqrt{d_{bg,i}}} e^{-jk_{ts}(\omega, \boldsymbol{\theta}_\ell)(d_{ts,i} + a)} \cdot \sum_{n=-\infty}^{+\infty} (-j)^n a_n H_n^{(2)}(k_{ts}(\omega, \boldsymbol{\theta}_\ell)d_{ts,i}) \quad (20)$$

where $G(j\omega)$ denotes the frequency spectrum of the incident wideband Gaussian modulated pulse, the first rational term describes the two-way propagation in the background, the second term denotes the forward propagation of a plane wave in the tissue, and the third summation term denotes the scattering by a tumor modeled as a dielectric cylinder [13]. d_{bg} and d_{ts} denote the propagation distances in the background medium and tissue, and k_{bg} and k_{ts} denote their frequency-dependent wave numbers, respectively. Here, $H_n^{(2)}$ denotes the n th-order Hankel function of the second kind and the coefficient a_n is given by

$$a_n = \frac{\frac{\omega \epsilon_m}{k_m} J_n(k_{ts}a) J_n'(k_m a) - \frac{\omega \epsilon_{ts}}{k_{ts}} J_n(k_m a) J_n'(k_{ts}a)}{-\frac{\omega \epsilon_m}{k_m} H_n^{(2)}(k_{ts}a) J_n'(k_m a) + \frac{\omega \epsilon_{ts}}{k_{ts}} J_n(k_{ts}a) H_n^{(2)'}(k_{ts}a)} \quad (21)$$

where ω is the angular frequency, a is the tumor radius, and k_m is the tumor wave number. ϵ_{ts} and ϵ_m are the relative permittivities of the healthy tissue and tumor, J_n denotes the n th-order Bessel function, and $(\cdot)'$ denotes the derivative with respect to the argument of the function. The effect of skin is not included in the model due to its small electrical size. This frequency-domain signal template is sampled with a 60-GHz sampling frequency and transformed to the time domain (512 samples).

For the MIT signal template, it is assumed that the tissue and the matching medium have the same acoustic properties. Thus, the elements of $\boldsymbol{\theta}_\ell$ additionally include the estimated average acoustic attenuation α_a and acoustic speed c_a . In order to model the finite sizes of the tumor and the acoustic transducer, the induced pressure is integrated among tumor region Ω and the transducer aperture Ψ , respectively. The time-domain signal template models the delay and attenuation, which is [9]

$$\mathbf{D}_i(t, \boldsymbol{\theta}_\ell) = \int_{\Psi} \int_{\Omega} \frac{e^{-\alpha_a |\mathbf{r}_i - \mathbf{r}_\ell|}}{\sqrt{|\mathbf{r}_i - \mathbf{r}_\ell|}} I \left(t - \frac{|\mathbf{r}_i - \mathbf{r}_\ell|}{c_a} \right) d\Omega d\Psi \quad (22)$$

where $I(t)$ is the signal modulating the sinusoidal plane wave.

IV. NUMERICAL SIMULATIONS

A. Breast Models

We consider 2-D circular numerical breast models with 80-mm diameter tissue enclosed by a 2.0-mm thick skin as shown in Fig. 1. The choice of the 2-D models is dictated by the limited computational resource: the simulations required for the MIT modality are too expensive to consider 3-D realistic breast models.

Human breast has irregular shape, which poses challenges for both the skin-breast artifact removal and the estimation of the distances of microwave propagation in each medium. Thus, the circular breast shape is adopted in this paper so that we can focus on the detection problem and leave the problem of irregular breast shape for future research. The dielectric properties of the tissue are derived from ten T-1 weighted MRI images [14] and are described by the one-pole Debye model with the relative permittivity for infinite value of frequency ϵ_∞ , the difference between the infinite and static relative permittivity $\Delta\epsilon$, the static conductivity σ_s , and the relaxation time constant τ [15].

TABLE I
TISSUE PROPERTIES FOR DATA SERIES

| Series # | Debye model parameters | | | | $\nu \times 100$ | $\min(\epsilon_{r,m}/\epsilon_{r,b})$ | $\max(\epsilon_{r,m}/\epsilon_{r,b})$ | $\min(\sigma_m/\sigma_b)$ | $\max(\sigma_m/\sigma_b)$ |
|----------|------------------------|----------------------|------------------|-------------|------------------|---------------------------------------|---------------------------------------|---------------------------|---------------------------|
| | $\epsilon_{\infty,b}$ | $\sigma_{s,b}$ (S/m) | $\Delta\epsilon$ | τ (ps) | | | | | |
| 1 | 3.1 | 0.05 | 1.6 | 13 | 7 | 10.6 | 11.1 | 24.8 | 25.1 |
| 2 | 4.0 | 0.08 | 3.5 | 13 | 30 | 6.4 | 7.7 | 11.5 | 11.9 |
| 3 | 4.0 | 0.08 | 3.5 | 13 | 40 | 6.3 | 8.0 | 11.5 | 12.0 |
| 4 | 13.0 | 0.4 | 24.4 | 13 | 30 | 1.4 | 1.6 | 1.7 | 1.8 |
| 5 | 13.0 | 0.4 | 24.4 | 13 | 50 | 1.3 | 1.7 | 1.7 | 1.8 |
| 6 | 13.0 | 0.4 | 24.4 | 13 | 70 | 1.3 | 1.7 | 1.7 | 1.8 |
| 7 | 13.8 | 0.7 | 35.6 | 13 | 10 | 1.1 | 1.2 | 1.2 | 1.2 |
| 8 | 13.8 | 0.7 | 35.6 | 13 | 30 | 1.1 | 1.2 | 1.2 | 1.2 |
| 9 | 14.2 | 0.8 | 40.5 | 13 | 10 | 1.0 | 1.1 | 1.0 | 1.0 |

TABLE II
MATERIAL PARAMETERS, WHERE “-” DENOTES A PIXELWISE MAPPING FROM THE MRI PIXEL INTENSITY VALUES TO THE PHYSICAL PROPERTIES

| | Unit | Background | Skin | Tissue | Tumour |
|---------------------|----------------------|------------|--------|--------|--------|
| ϵ_{∞} | | 4.8 | 15.93 | - | 6.75 |
| σ_s | (S/m) | 0.0 | 0.831 | - | 0.79 |
| $\Delta\epsilon$ | | N/A | 23.83 | - | 48.35 |
| τ | (ps) | N/A | 13 | 13 | 10.47 |
| c_a | (m/s) | 1452 | 1615 | - | 1550 |
| α_a | (dB/m) | 95 | 35 | 45 | 41 |
| ρ | (kg/m ³) | 950 | 1100 | 1020 | 1182 |
| c_p | J/(kg·K) | 1800 | 3680 | 2220 | 3500 |
| α | 1/K | 6.3e-4 | 3.0e-4 | 3.0e-4 | 3.0e-4 |

For the background, ϵ_r is given in place of ϵ_{∞} .

In order to cover a range of possible average dielectric properties of the healthy breast tissue, we consider $N_s = 9$ series of numerical breast models and we take the tissue properties defined by the Debye model from [16]. Table I contains the parameters of the models: $\Delta\epsilon$ and τ have been fixed to constant values while ϵ_{∞} have been assigned values by linearly mapping the grayscale MRI pixel intensity as

$$\epsilon_{\infty}(p) = \epsilon_{\infty,b} \left(1 + \frac{\nu}{2} - \frac{M(p) - \min(M)}{\max(M) - \min(M)} \nu \right) \quad (23)$$

where p is the pixel number in the MRI image M and in the corresponding material map; ν denotes the percent of variation, which defines the level of heterogeneity (see Table I). Exactly the same expression applies to map σ_s . Table II depicts the exact values of the tissue properties that we use for modeling [17]. The last four columns of Table I represent the resulting statistics of the generated material maps: the minimum and maximum ratios of the dielectric properties of malignant to benign tissues evaluated at the central frequency 6.85 GHz using the Debye model. In the considered scenario, the breast has been immersed in an oil-like coupling medium with $\epsilon_r = 4.8$.

Five acoustic and thermal properties associated with the breast models have been compiled from [14], [18], and [19] and are listed in Table II. Density ρ , acoustic attenuation α_a , heat capacity c_p , and volume expansion coefficient α are assumed constant for each of the propagation media. Acoustic speed c_a is variable to capture the acoustic heterogeneity of the

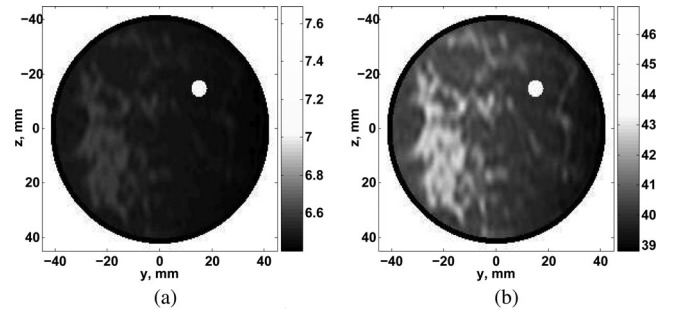


Fig. 2. Dielectric properties of the numerical breast models evaluated at 6.85 GHz (series #8, tumor at location T2). (a) Conductivity. (b) Permittivity.

breast tissue. It has been mapped from the MRI pixel intensities using (23) with $\nu = 0.1$ and $c_{a,b} = 1510$ m/s.

Ten (N_t) different realizations of tissue structure (H1, ..., H10) have been used for each of the nine series. H2, ..., H10 have been utilized as the training set to capture the distribution of the tissue clutter while H1 has been left to build two tumorous breast models by placing a circular tumor ($R = 3$ mm) inside the breast tissue at two positions relative to the center of the breast: $[-20$ mm; 8 mm] (T1) and $[15$ mm; -15 mm] (T2). These are chosen to illustrate an easier case (adipose-dominant area) and a more difficult one (tumor location for T1 has a higher tissue density, which decreases the dielectric contrast and makes the detection task more difficult). Overall, $N_s \times N_t = 9 \times 10 = 90$ healthy and $N_s \times 2 = 9 \times 2 = 18$ tumorous breast models have been considered in this study. An example of the distribution of the permittivity and conductivity for series #8 (tumor location T2) is shown in Fig. 2.

B. MR Simulations

In the MR simulation, as shown in Fig. 1(a), transverse-magnetic Gaussian-modulated sinusoidal plane waves polarized in the $+x$ direction [directed from this paper toward the reader as in Fig. 1(a)], with a 3-dB bandwidth of 7.5 GHz are launched toward a breast model at $M = 36$ equally spaced angles. We use the FDTD method to solve Maxwell's equations and implement the plane wave using the analytic field propagator method [20]. The spatial increment is set to 0.4 mm, which leads to 475×450 Yee's cells. We place ten perfectly matched layers to truncate

the scattered field region. The result is a vector of scattered signal recorded at each of the M antennas working in the receiving mode.

C. MIT Simulations

In the MIT simulation as shown in Fig. 1(b), plane waves at 800 MHz are launched toward the breast model at $M = 36$ angles. Each simulation runs for eight periods to reach the time-harmonic steady state. We use the two-point estimation method [21] to calculate the amplitude of the electric field E_x , and use

$$S(\mathbf{r}) = \frac{\sigma(\mathbf{r})|E_x(\mathbf{r})|^2}{2\rho(\mathbf{r})} \quad (24)$$

to calculate the pointwise specific absorption rate. The wavelength at 800 MHz in the coupling medium is 171 mm, which is two times larger than the dimension of the breast models. The nonuniform heating due to the comparable electric size of the breast is inherently included in this simulation. Our calculation of the specific absorption rate shows that its variability across the breast domain reaches 15 dB.

The specific absorption rate is interpolated from the coarse grid for the electromagnetic simulations to the dense grid for the acoustic simulations. The thermoacoustic wave equation is

$$\nabla^2 p - \frac{1}{c_a^2} \frac{\partial^2 p}{\partial t^2} = -\frac{\alpha}{c_p} \frac{\partial}{\partial t} S(\mathbf{r}) I(t) \quad (25)$$

where p denotes the pressure. The right-hand side of this equation is the spatially dependent specific absorption rate multiplied by the temporal envelope $I(t)$, which is a Gaussian function with a 10-dB bandwidth of 1.1 MHz. The spatial increment is set to 0.1 mm, which leads to 1600×1600 Yee's cells. We truncate the simulation domain with 20 perfectly matched layers. Each acoustic simulation captures a time span of $150 \mu\text{s}$.

In order to reflect realistic measurement equipment, we add Gaussian measurement noise to the acquired signals (on the order of -60 dB relative to the signal maximum).

V. RESULTS AND DISCUSSION

For evaluation purposes, we use the *peak-to-sidelobe ratio* (PSLR) metric, defined as follows:

$$\text{PSLR} = 20 \log(I_{\max,s}/I_{\text{s1}}) \quad (26)$$

where I_{s1} is the most significant sidelobe amplitude of a tumorous image. The contrast in the dielectric properties between tumorous and healthy tissue is correlated with the contrast of the breast images. The imaging algorithms cannot completely isolate the reflection due to the synthetic focal point. This leads to the presence of sidelobes in the images. PSLR is a metric to evaluate how well the imaging algorithms can preserve the dielectric contrast.

Each of the considered series 1, \dots , 9 comprises two tumorous cases (T1 and T2) and a corresponding healthy scenario (H1). We compute four images of test statistics, for each of these cases, as described in Section III-B: $U(\tilde{\mathbf{x}})$, $V(\tilde{\mathbf{y}})$, $Z(\tilde{\mathbf{x}}, \tilde{\mathbf{y}})$, $W(\tilde{\mathbf{x}}, \tilde{\mathbf{y}})$. Fig. 3 illustrates examples of images obtained as the

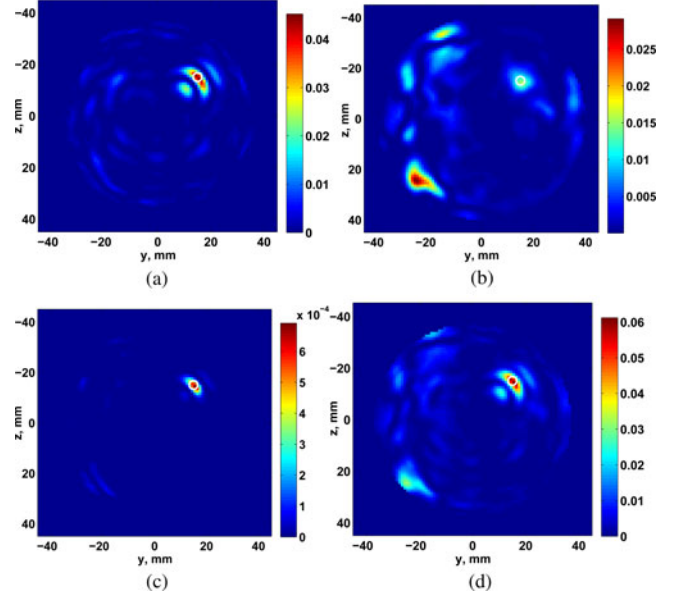


Fig. 3. Examples of images for the four types of test statistics (note improvement in clutter suppression for W). Actual tumor location is shown by a circle (tumor position T2). (a) U . (b) V . (c) W . (d) Z .

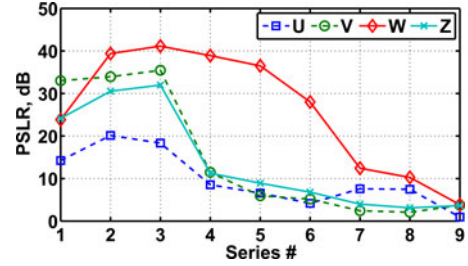


Fig. 4. Averaged peak signal-to-sidelobe ratio versus the series number (see Table I). The W test statistic provides high performance to reduce the effects of clutter for series 2 \dots 8.

output of the GLRT algorithm corresponding to the breast models depicted in Fig. 2. The pixels represent the test statistic values at locations $\{r_\ell\}_{\ell=1}^L$ on the grid with spatial resolution of 1 mm. With the 1-mm grid, around 5100 test locations inside the breast region have been assigned values.

The difference in the spatial distribution of clutter between U and V test statistics is noticeable, which is the principal property that the fusion benefits from. The W test statistics displays considerable clutter suppression [see Fig. 3(c)]. The clutter- and sidelobe-reduction effects of the W test statistic are also evident in the PSLR metric (see Fig. 4).

The W test statistic provides high clutter-reduction performance for series 2, \dots , 8.

The next stage of the tumor detection technique is thresholding. We set the thresholds based on an estimated distribution for the healthy cases with the goal of minimizing the false discovery rate (FDR). The software package quality [22] was used to estimate the false discovery rate with respect to the test statistics. For one healthy and two tumorous cases available for each series, we used the odd-one-out approach to set the threshold, i.e., first we estimated the threshold based on the values of the

TABLE III
DETECTION PERFORMANCE FOR THE THRESHOLDS GIVEN
BY THE QUALITY TOOL

| | U | V | W | Z |
|--------------|-----|-----|-----|-----|
| False alarms | 2 | 1 | 0 | 0 |
| Misses | 6 | 8 | 5 | 5 |

The results correspond to tests on 90 healthy cases and 18 tumorous cases

test statistics for cases T2, H2, . . . , H10 and applied it to the test cases T1 and H1; next, the threshold was obtained from T1, H2, . . . , H10 cases and applied to the test cases T2 and H1. The value of the test statistic with minimum positive q -value was used as the threshold.

Table III summarizes the detection performance achieved using the described methodology. The values in the table were obtained as follows. Thresholds calculated for each series and mode were applied to the corresponding two tumorous cases and one healthy case. If in the resulting images, pixels of the test statistic in the tumorous area remained above the threshold, this case was considered as a “hit.” Otherwise, the result was considered as a miss. Similarly, if after thresholding of cases H1 (with the two thresholds) some pixels remained above the thresholds, it was considered as a false alarm. The tumorous area was defined as follows: the circle of 10-mm radius around the image maximum in case of correct localization; or the same circle around the actual tumor location in case the localization was not correct for a given case. The localization was defined as correct in case the image maximum was within the 10-mm radius from the actual tumor location. The total number of misses along all the series for T1 and T2 cases was calculated and inserted into Table III. The total number of false alarms summed up along the series is shown in the corresponding columns. Improvement in detection performance for both W and Z test statistics can be seen.

Since we penalize FDR, the number of false alarms is lower than the number of misses. However, both the number of misses and the number of false detections are less for the fusion approach than for any of the component approaches, as follows from Table III. This demonstrates the utility of the proposed approach. If another criterion is used to set the threshold, for example, minimization of the probability of type II error (probability of a miss), we could achieve better results in the number of misses, but, most likely, the number of false alarms would increase in this situation. The investigation of the different thresholding approaches will be considered in future work.

VI. CONCLUSION

We proposed a dual-modality approach to fuse data from the methods of MR and MIT. In a hypothesis testing framework, we identified two test statistics, one based on the GLRT and one heuristic. We derived the null distributions of these statistics to enable the selection of thresholds and evaluated their performance using FDTD-simulated signals. The fusion approach can decrease the number of false alarms (detection of tumor when it is not present) and misses (failure to detect tumor that is present). Although limited in statistical significance, these re-

sults indicate that benefit can be derived from using the MR and MIT modalities jointly, in a manner that allows fusion of their signals.

REFERENCES

- [1] E. Fear, X. Li, S. Hagness, and M. Stuchly, “Confocal microwave imaging for breast cancer detection: Localization of tumors in three dimensions,” *IEEE Trans. Biomed. Eng.*, vol. 49, no. 8, pp. 812–822, Aug. 2002.
- [2] R. A. Kruger, K. Stantz, and W. L. Kiser, Jr., “Thermoacoustic CT of the breast,” in *Proc. SPIE Conf. Med. Imag.: Phys. Med. Imag.*, Feb. 2002, vol. 4682, pp. 521–525.
- [3] M. Xu and L. Wang, “RF-induced thermoacoustic tomography,” in *Proc. IEEE Annu. Conf. Biomed. Eng. Soc.*, 2002, vol. 2, pp. 1211–1212.
- [4] E. J. Bond, X. Li, S. C. Hagness, and B. D. van Veen, “Microwave imaging via space-time beamforming for early detection of breast cancer,” *IEEE Trans. Antennas Propag.*, vol. 51, no. 8, pp. 1690–1705, Aug. 2003.
- [5] S. K. Davis, H. Tandradinata, S. C. Hagness, and B. D. van Veen, “Ultra-wideband microwave breast cancer detection: A detection-theoretic approach using the generalized likelihood ratio test,” *IEEE Trans. Biomed. Eng.*, vol. 52, no. 7, pp. 1237–1250, Jul. 2005.
- [6] T. Williams, E. Fear, and D. Westwick, “Tissue sensing adaptive radar for breast cancer detection—Investigations of an improved skin-sensing method,” *IEEE Trans. Microw. Theory Tech.*, vol. 54, no. 4, pp. 1308–1314, Jun. 2006.
- [7] M. Klemm, I. J. Craddock, J. A. Leendertz, A. Preece, and R. Benjamin, “Radar-based breast cancer detection using a hemispherical antenna array—Experimental results,” *IEEE Trans. Antennas Propag.*, vol. 57, no. 6, pp. 1692–1704, Jun. 2009.
- [8] Y. Xie, B. Guo, L. Xu, J. Li, and P. Stoica, “Multistatic adaptive microwave imaging for early breast cancer detection,” *IEEE Trans. Biomed. Eng.*, vol. 53, no. 8, pp. 1647–1657, Aug. 2006.
- [9] Y. Xie, B. Guo, J. Li, G. Ku, and L. V. Wang, “Adaptive and robust methods of reconstruction for thermoacoustic tomography,” *IEEE Trans. Biomed. Eng.*, vol. 55, no. 12, pp. 2741–2842, Dec. 2008.
- [10] S. Kay, *Fundamentals of Statistical Signal Processing, Volume 2: Detection Theory*. Englewood Cliffs, NJ: Prentice-Hall, 1998.
- [11] B. Oreshkin, E. Kirshin, G. K. Zhu, M. Popovic, and M. Coates. (2011). *Null hypothesis distributions of the test statistics for the dual-modality fused detection* [Online]. Available: <http://www.tsp.ece.mcgill.ca/Networks/publications-techreport.html>
- [12] V. Adamchik and O. Marichev, “The algorithm for calculating integrals of hypergeometric type functions and its realization in reduce system,” in *Proc. ACM Int. Symp. Symbolic Algebr. Comput.*, 1990, pp. 212–224.
- [13] R. F. Harrington, *Time-Harmonic Electromagnetic Fields*. Piscataway, NJ: IEEE Press, 2001.
- [14] J. L. Prince and J. M. Links, *Medical Imaging Signals and Systems*. Englewood Cliffs, NJ: Prentice-Hall, 2006.
- [15] A. Sihvola, *Electromagnetic Mixing Formulas and Applications*. London, U.K.: Institution of Electrical Engineers, 1999.
- [16] E. Zastrow, S. K. Davis, M. Lazebnik, F. Kelcz, B. D. van Veen, and S. C. Hagness. (2007). *Database of 3D grid-based numerical breast phantoms for use in computational electromagnetics simulations* [Online]. Available: <http://uwcem.ece.wisc.edu/MRI/database/InstructionManual.pdf>
- [17] M. Lazebnik, M. Okoniewski, J. H. Booske, and S. C. Hagness, “Highly accurate Debye models for normal and malignant breast tissue dielectric properties at microwave frequencies,” *IEEE Microw. Wireless Compon. Lett.*, vol. 17, no. 12, pp. 822–824, Dec. 2007.
- [18] N. P. Laboratory. *Kaye and Laby tables of physical and chemical constants* (1995). [Online]. Available: <http://www.kayelaby.npl.co.uk>
- [19] F. A. Duck, *Physical Properties of Tissue: A Comprehensive Reference Book*. San Diego, CA: Academic Press, 1990.
- [20] J. B. Schneider, “Plane waves in FDTD simulations and a nearly perfect total-field/scattered-field boundary,” *IEEE Trans. Antennas Propag.*, vol. 52, no. 12, pp. 3280–3287, Dec. 2004.
- [21] U. Oğuz and L. Gürel, “Interpolation techniques to improve the accuracy of the plane wave excitations in the finite difference time domain method,” *Radio Sci.*, vol. 32, pp. 2189–2199, 1997.
- [22] L. Käll, J. Storey, and W. Noble, “Quality: Non-parametric estimation of q -values and posterior error probabilities,” *Bioinformatics*, vol. 25, pp. 964–966, Jan. 2009.

Authors’ photographs and biographies not available at the time of publication.